Available online at www.sciencedirect.com

SciVerse ScienceDirect

Journal of the European Ceramic Society 32 (2012) 633–641

www.elsevier.com/locate/jeurceramsoc

Processing of nano-SiC ceramics: Densification by SPS and mechanical characterization

F. Lomello [a,*], G. Bonnefont [b], Y. Leconte [a], N. Herlin-Boime [a], G. Fantozzi [b]

[a] DSM/IRAMIS/SPAM/LFP(CEA CNRS URA 2453) CEA Saclay, Bât. 522, 91191Gif-sur-Yvette, France

[b] Université de Lyon, INSA de Lyon, MATEIS UMR CNRS 5510, Bât. Blaise Pascal, 7 Av. Jean Capelle, 69621 Villeurbanne, France

Received 15 August 2011; received in revised form 27 September 2011; accepted 1 October 2011

Available online 21 October 2011

Abstract

β-SiC nanopowders with a mean particle size of 16.6 nm were obtained by laser pyrolysis. De-agglomeration of the powder was performed in an aqueous medium under magnetic stirring and ball-milling. Subsequently, green bodies were prepared by slip-casting of slurries. In this context, non-conventional densification routes such as Spark Plasma Sintering (SPS) with an applied pressure of 70 MPa allowed to achieve high final densities (96% TD). Different microstructures were obtained by varying the sintering temperature. Finally, the mechanical properties of the samples (hardness, toughness) were determined and a correlation between the final microstructures and the mechanical behavior was established.

Keywords: SiC; Spray-pyrolysis; Dispersion; Spark plasma sintering; Mechanical properties; Nuclear applications

1. Introduction

Ceramic carbides materials such as SiC, due to their refractory nature and their low neutron absorption are believed to be promising candidates (as bulk, coating or in composites) for manufacturing the fuel cladding for the future generation of nuclear fission reactors.[1] Furthermore, SiC represents a potential material as first-wall material in fusion reactors.[2–4]

However, SiC brittleness has limited its structural application. For counteracting this phenomenon, a reduction of grain size (below 100 nm) together with a high final density (also for fission products retention) seems to be the solutions for improving mechanical properties. Moreover, the reduced grain size may enhance the resistance to irradiation as reviewed in literature.[5]

Sintering additives are usually employed for SiC sintering, generally boron-based or yttrium and aluminum oxides, in order to achieve high densities and fine grain sizes. The presence of additives allows to improve the mechanical properties,[6] although they present drawbacks under irradiation (neutron absorption or swelling). Oxide phase at grain boundaries can also impede mechanical performances at high temperatures. In order to avoid these drawbacks, no sintering additives were used in the presented study.

In order to obtain fine grained ceramics, the starting powders grain size has to be decreased down to the nanometric scale. Laser pyrolysis is known to be an interesting technique for producing various carbide nanopowders.[7] This latter technique already developed for large production rates (more than 2 kg/h for SiC) has been extensively studied since its development for the synthesis of SiC.[8,9] Gaseous process using the decomposition of silane mixed with a gaseous carbon precursor as acetylene or ethylene allows to control the final grain size and degree of crystallization.[10]

However, gas phase synthesized nanopowders are usually agglomerated and this affects the green samples forming by generating porosity. In the green state, two types of pores exist: the inter-agglomerate pores (microns) and intra-agglomerate pores (nanometers). The elimination of the micronic inter-agglomerate pores requires high densification temperatures promoting the grain growth.[11,12]

In this context, the dispersion of the initial nanopowders carried out by magnetic stirring or ball-milling seems to be a key in reducing the initial agglomeration.[13] The second beneficial effect introduced by the dispersion process can be the mechanical activation which is likely to increase the density of surface

* Corresponding author. Tel.: +33 1 69 08 69 16; fax: +33 1 69 08 87 07.
E-mail address: fernando.lomello@cea.fr (F. Lomello).

0955-2219/$ – see front matter © 2011 Elsevier Ltd. All rights reserved.
doi:10.1016/j.jeurceramsoc.2011.10.006

defects and as a consequence to enhance the sinterability as it was shown by Ohyanagi et al.[14]

Moreover, employing non-conventional sintering routes such as SPS allows reaching high fired densities at short sintering times, thus minimizing the grain growth.[15] Recently, some interesting mechanical values regarding nano-SiC sintered by SPS were found by Yamamoto et al.[16]

In this work, β-SiC produced by laser pyrolysis was submitted to magnetic stirring and ball-milling. Then, green bodies were prepared by slip-casting and uniaxially pressed at 188 MPa prior to SPS sintering.

Standard mechanical characterization (hardness and toughness) of sintered samples was conducted. The aim of this study was to establish a correlation between the microstructural features and the mechanical behavior.

2. Material and methods

SiC synthesis was achieved from a gaseous mixture of silane SiH_4 and acetylene C_2H_2. During the synthesis, SiH_4 and C_2H_2 flows were set at 395 sccm and 190 sccm, respectively. The aim was to obtain a Si/C ratio leading to a slight excess in Si in the final product in order to favor the powder dispersion in water through the formation of surface Si-OH bonds. Laser power was 600 W and the process pressure was kept constant at 740 Torr. The production rate was 35.8 $g.h^{-1}$.

Physico-chemical characterization of as-produced powder was conducted. Chemical analyses were performed with a relative uncertainty of 3%. Si content was measured by ICP-AES at CNRS central analysis laboratory (Vernaison, France). C content was measured with Horiba EMIA-320 V apparatus, while O content was measured with Horiba EMGA-820 apparatus. Powders were submitted to X-ray diffraction (XRD, Philips X'Pert) using the Cu Kα1 radiation (λ = 1.5406 Å). In order to determine the particle average size, TEM observations (Topcon 02B) were performed on the as-produced powder. True density of the starting powder was estimated from chemical composition (detailed later) and was confirmed by helium pycnometry measurements (Micrometrics Accupyc 1330). Specific surface area was measured on a Micrometric Automate 23 apparatus after outgassing at 150 °C for 1 h.

Powders were submitted to suitable dispersion processes in distilled water with a solid content of 30 wt%. The dispersion was conducted by magnetic stirring for 200 h or pseudo ball-milling for 100 h (powder/spheres ratio 1:50, Union Process SiC Satellites of 3/16″). Samples are labeled in the paper as MS when dispersed by magnetic stirring and BM when dispersed by pseudo ball-milling. This latter process is obtained by shaking the powders/balls slurry in a mixing device (Turbula Type T2F, Willy A. BachofenMaschinenfabrik AG, Switzerland) at 72.7 r.p.m.

During dispersion Dolapix A 88 (2-amino 2-methyl propanol) supplied by Zschimmer & Schwarz, Germany was added as dispersant. The concentration was 3.5 wt%. The deflocculating effect of this pseudo cationic dispersant on SiC particles surface generates charges of same polarity which provokes the repulsion of particles.

In order to check the efficiency of the dispersion step, grains and agglomerates sizes were measured by photon correlation spectroscopy (PCS) by means of MalvernZetasizer 300 HS apparatus.

After dispersion, slurries were slip-casted in porous ceramic molds and uniaxially pressed at 188 MPa with the aim of increasing the green density. These green densification values were calculated taking into account the starting density value (true density) measured by helium pycnometry on as synthesized nanopowders.

The powders were sintered by using SPS equipment HPD 25/1 (FCT System GmbH, Germany). The following sintering parameters have been used:

- General conditions: a graphite die with an internal diameter of 20 mm and a wall thickness of 10 mm was used with 2 g of powder. A graphite felt with a thickness of 8 mm surrounded the matrix in order to avoid thermal losses. A pressure of 73 MPa was applied at the beginning of the cycle during 30 s at room temperature and then, it was released and a constant pressure of 16 MPa was applied up to 1450 °C. Then, the pressure was increased up to 73 MPa. This pressure was released at the end of the holding time.

All the experiments were made under a vacuum of 1 Pa. The following pulse sequence was chosen: 10 ms of pulsed current followed by 5 ms of current without pulse. The cooling rate corresponded to a natural cooling. The heating rate was fixed at 185 °C/min and the soaking time at the sintering temperature (from 1700 to 1900 °C) was 5 min.

The temperature was measured by means of an optical pyrometer focused on the upper graphite punch, at about 4 mm from the sample. Sintered samples exhibited a thickness of 2 mm.

The following flow chart illustrates the fabrication process (Fig. 1) employed for producing nano-SiC ceramics.

Bulk densities were measured by Archimedes method following the C373-88(2006) ASTM standard test method as well as by helium pycnometry. The degree of densification (density of the sintered part compared with the theoretical density) was calculated taking into account the content of the single elements after chemical analysis performed on sintered pellets. Vickers Hardness (HV) measurements were carried on surfaces polished with diamond paste down to 3 μm using a Vickers Hardness Tester FV-7 with an applied force of 10 daN held for 15 s. The obtained values were the average over five measurements. Fracture toughness was estimated using the Anstis formula.[17] Microstructural features on sintered samples were analyzed by SEM (Zeiss Ultra-55 Scanning Electron Microscope) on the fracture surfaces. These SEM observations enabled the grain size measurement by using image analysis software (ImageJ).[18] The mean value was calculated by using the average linear intercept method in the horizontal and vertical directions on at least a hundred grains.

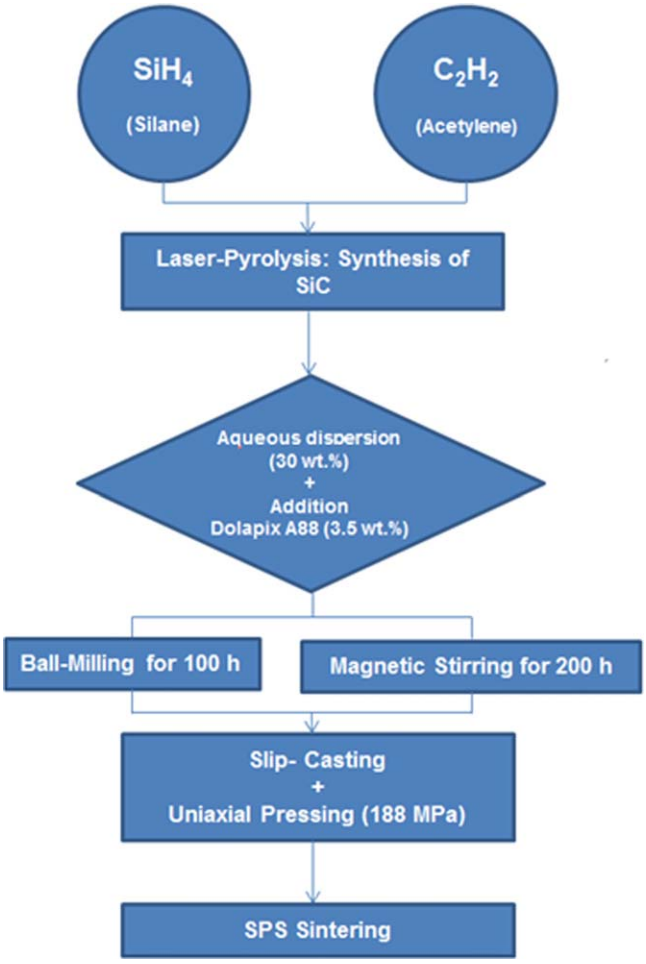

Fig. 1. Schematic flow-chart of the nano-SiC preparation.

3. Results

3.1. Starting powder structure

The physico-chemical features of the as-produced powder are summarized in Table 1.

Chemical analyses indicated that the as-produced powder contains free-carbon and oxygen since, theoretically, SiC is composed of 70 wt% Si and 30 wt% C. Indeed, the true density can be calculated by knowing the elements content. In order to achieve this estimation, the O present in the sample was assumed to be bonded to Si as SiO_2 phase. The Si amount involved in this silica phase was subtracted to the total Si amount. Remaining Si amount was assumed to be bonded to C as SiC phase. The C amount involved in this carbide phase was subtracted to the total C amount. The remaining C content was considered as free C. Finally, a value of 3.05 g/cm^3 was calculated following these approximations, this value will be later referred as the true density. A nearby value of 3.02 g/cm^3 was measured by helium pycnometry, showing that the calculation from chemical composition was relevant.

Table 1
Physico-chemical properties of the as-produced powder.

Average particle size (TEM)	16.6 nm
SSA (BET)	114 m^2/g
True density	3.02 g/cm^3
Crystal phase	β
Si (wt%)	65.7%
C (wt%)	29.2%
O (wt%)	5.0%

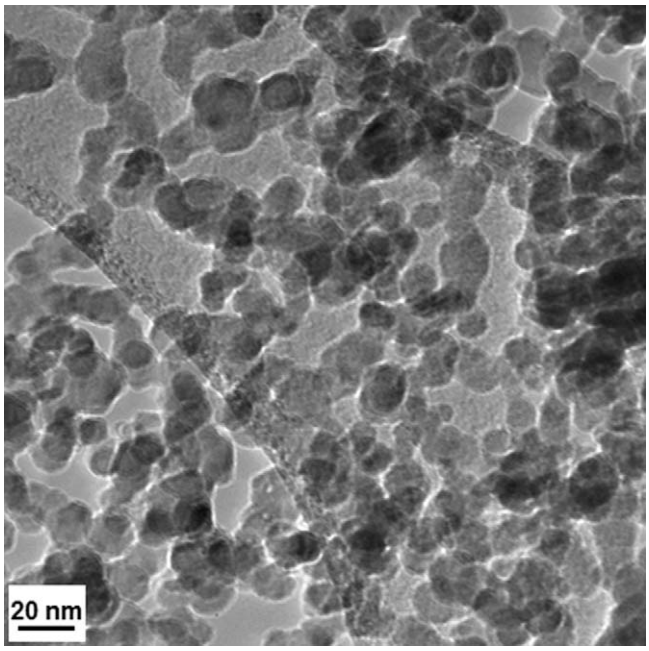

Fig. 2. TEM micrograph of the as-produced powder.

The relatively high O content cannot be ascribed to pollution during the SiC grain growth, as the purity of the precursor gases (electronic grade) and the leak proofness of the reactor avoid any possible O contamination. The high O content is the consequence of multiple factors enhancing the oxidization after synthesis: high specific surface, air processing for powder collection and treatment, and in this particular case Si excess in the Si/C ratio.

The specific surface area (SSA) was measured at 114 m^2/g. Assuming a spherical shape and using the true density ρ, a corresponding grain size D can be estimated through the following relation:

$$D = \frac{6}{\rho \mathrm{SSA}} \quad (1)$$

The estimated grain size from SSA measurements is then 17.3 nm. This can be compared to the mean grain size estimated from TEM picture shown in Fig. 2. The average size is found at 16.6 nm, with a size distribution ranging from 5.1 to 26.5 nm. This is in good agreement with the value estimated from BET measurements, taking into account that these latter ones come with experimental uncertainty.

Fig. 2 also shows that the powder is composed by very fine grains exhibiting a chain-like agglomeration.

The XRD pattern revealed that powder is exclusively composed by the cubicphase β-SiC (JCDD #74-2307) as shown in Fig. 3.

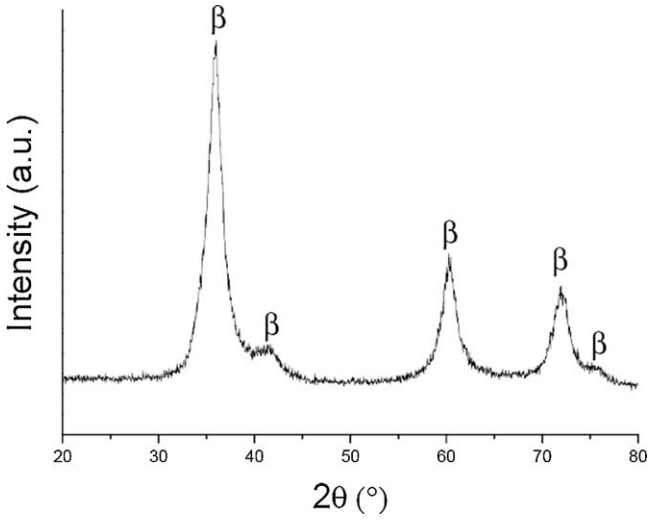

Fig. 3. XRD pattern of the as-produced powder.

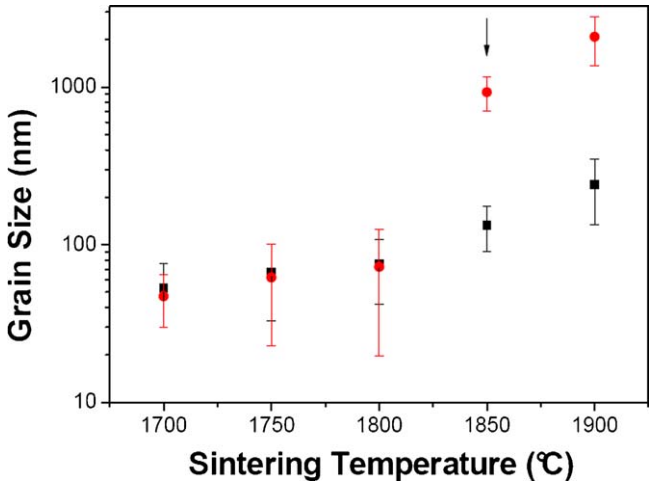

Fig. 5. Evolution of the grain size as a function of the sintering temperature (■, magnetic stirring; •, ball milling). The arrow indicates the excessive grain growth.

The XRD analysis permits to calculate the crystallites size by applying the Scherrer's method. This is a rough estimation of the crystallite size, as the fitting method used to determine the full width at half maximum (FWHM) of the diffraction peaks cannot take correctly into account the shape resulting of crystallite size distribution. This estimation also considers the absence of strain broadening in the diffraction peaks (which is commonly assumed for powders), which could lead to underestimate the final crystallite size in nanometric particles. Nevertheless, the calculated value was 13.5 nm indicating that the crystallite size is relatively close to the particle size observed by TEM. This seems to indicate that the powder is constituted by single crystalline grains.

As previously mentioned, two dispersing routes were employed in this study (MS and BM). In terms of agglomerate size after process, both routes gave similar results. These results are shown in Fig. 4. After dispersion, a bimodal distribution, corresponding to the distribution in volume was measured. In point of fact, a broad peak at 24.1 nm accompanied by a second at 147 nm were observed. An important reduction of equivalent agglomeration distribution was thus achieved. The small size population (24.1 nm) can indeed be ascribed to individual primary particles, as PCS gives the hydrodynamic gyration radius value, taking into account the particle diameter surrounded by surfacting species and solvatation layer. Moreover, volume distribution is highly sensitive to the presence of very few larger agglomerates which diffuse light very efficiently: in terms of number of bodies, the population around 147 nm would be very weak. The distribution in number is also reported in Fig. 4.

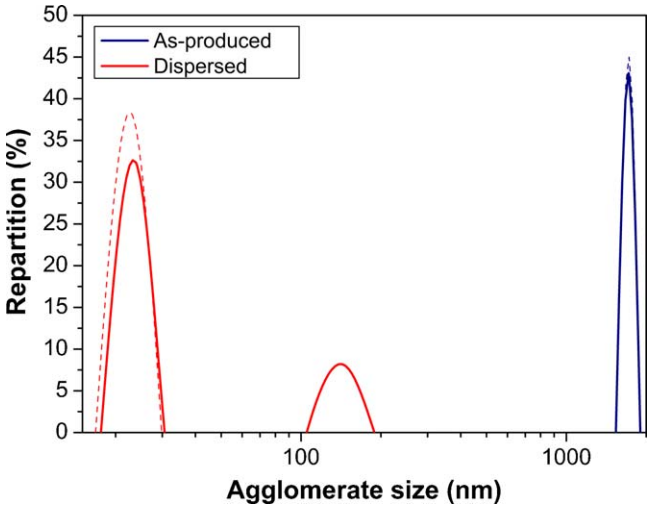

Fig. 4. Photon correlation spectroscopy (PCS) size distribution of magnetically-stirred sample (MS): in volume (solid line) and in number (dashed line).

3.2. Sintering

Samples were sintered in the 1700–1900 °C range, in order to obtain different microstructure developments. Samples exhibited a green density of about 1.51 and 1.43 g/cm^3 for MS and BM corresponding to 50.0% and 47.3% of TD, respectively. The relative density was calculated on the basis of the true powder density (3.05 g/cm^3) taking into account the oxygen content, 5.0 wt%.

Indeed, the oxygen content limited the success in developing SiC nanoceramics as it has a detrimental effect on the coarsening and densification. A reduction of the dihedral angle in SiO_2-coated SiC nanoparticles was observed by several authors.[19] During sintering, SiO_2 can be reduced from 1500 °C as two reactions (Eq. (2)) could take place leading to the SiO formation.

$$\begin{aligned} &SiO_2 + C(s) \rightarrow CO(g) + SiO(g) \\ &2SiO_2(s) + SiC(s) \rightarrow CO(g) + 3SiO(s) \end{aligned} \quad (2)$$

If SiO is still present in the powder, it promotes the sintering by vapor transport which promotes the neck formation and grain growth.[20] Nevertheless, formation and release of gaseous SiO can favor the appearance of porosity.

In Fig. 5, grain sizes of the different sintered samples are presented. As represented on the figure, sample BM exhibited an abnormal grain growth from 1850 °C.

Table 2
Oxygen content of dispersed and sintered samples.

Sample	Oxygen content (wt%)
Dispersed MS	6.1
MS sintered at 1900 °C	0.7
Dispersed BM	6.6
BM sintered at 1900 °C	0.8

In order to discriminate the effect of the oxygen on the grain growth, chemical analyses were performed on the dispersed and sintered samples. In Table 2, the oxygen content of all samples is presented.

After dispersion, an increase up to >6 wt% due to the prolonged dispersion in an aqueous medium was observed. On the other hand, after sintering a reduction down to <1 wt% was found. The reductive SPS conditions are effective to decrease the oxygen content through several possible reactions: formation of gaseous SiO (see Eq. (2)) or formation of CO and CO_2 generated by oxidization of free C, graphite and organic dispersing agent. Concerning the explanation of the different behavior upon sintering in MS and BM samples, the O effect cannot be responsible as the content in this element is similar in both powders after dispersion. Thus, physical surface activation during the milling process may be responsible for the grain coarsening as no significant differences were found in terms of oxygen content in green samples.

Taking into account the oxygen content after sintering, the theoretical density could be calculated. Considering the chemical composition, if the pellets had been densified at 100%, their density for both dispersion routes would be 3.15 g/cm^3 which differs from the theoretical value of 3.21 g/cm^3. For this reason, fired densities were calculated employing the analytical calculated value of 3.15 g/cm^3.

In Fig. 6, the evolution of density as a function of the sintering temperature is presented.

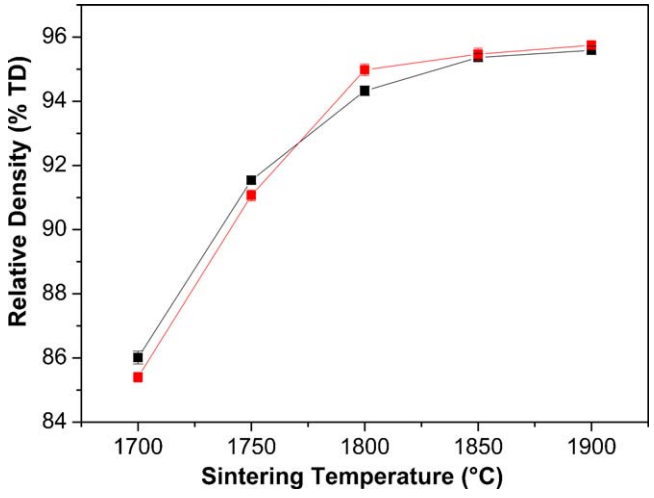

Fig. 6. Evolution of the density as a function of the sintering temperature (■, magnetic stirring; ●, ball milling).

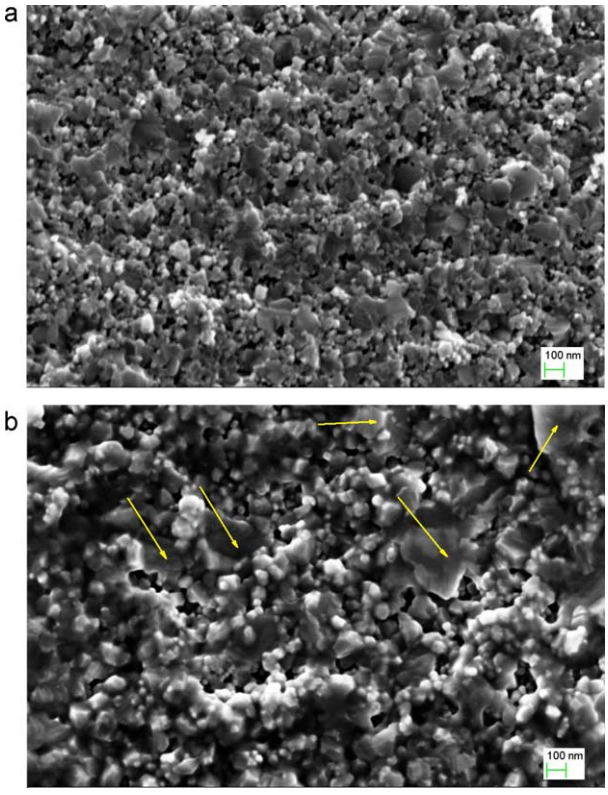

Fig. 7. SEM micrographs at the same magnification (100k×) of the fracture surfaces ofmagnetically-stirred samples (MS): Sintered at 1750 °C (a) and 1900 °C (b).

A similar densification was obtained by both dispersion routes. However, a slight anticipation in BM at 1800 °C was observed.

3.3. Microstructural characterization

In Figs. 7 and 8, some SEM micrographs are presented. Micrographs were taken at the center of the specimens. Samples sintered at 1750 °C exhibit a fine grained microstructure consisting of round-shaped grains of 60–70 nm entrapping diffuse residual porosity. The fracture mode is radically different: in case of MS it is prevalently intergranular while BM presented both inter- and transgranular modes. Transgranular fracture zones are indicated with arrows.

Samples sintered at 1900 °C present quite different microstructural features. MS sample is still composed of fine grains of about 240 nm. In contrast, BM sample is characterized by a large grain growth (≈2 μm). The unexpected coarsening should be imputable to the surface activation as similar oxygen content was found in both samples. During the grain size measurement in BM 1900 °C sample, some difficulties were faced as the crack propagation was mostly transgranular which probably leads to an overestimation of the average grain size.

3.4. XRD pattern of the sintered samples

An interesting aspect was found through XRD analysis of all sintered samples (namely in MS and BM). It is illustrated

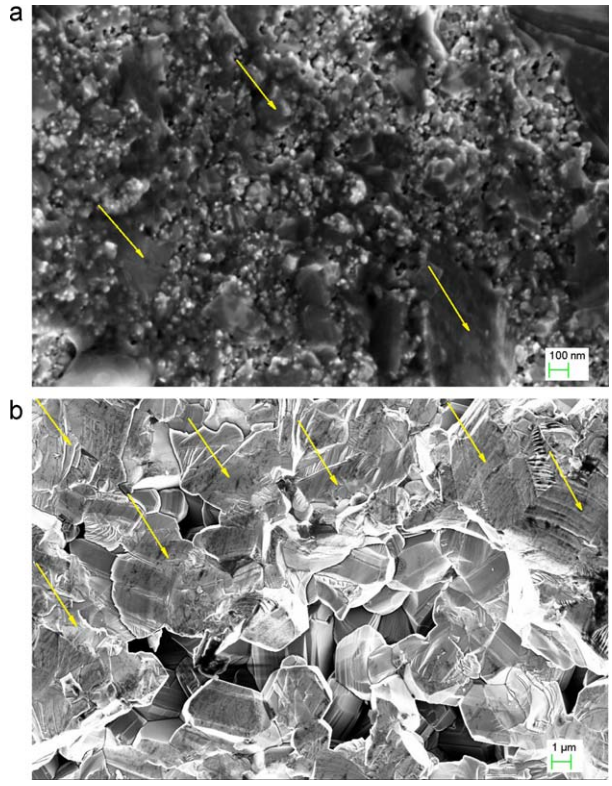

Fig. 8. SEM micrographs of the fracture surfaces at different magnifications (100k× and 10k×) of ball-milled samples (BM): sintered at 1750 °C (a) and1900 °C (b).

in Fig. 9. Sintered samples are composed by two phases: the main β-SiC (JCPDF # 074-2307) and a secondary pure Si phase (JCPDF # 075-0590), indicating an excess in Si content already present in the as-produced powder but previously not detected by XRD.

In sintered samples a low intensity peak near 33.6° (1 0 0)-indicated with an arrow in the XRD pattern – corresponds to non-symmetric reflection related to stacking or planar faults (twin boundaries) as reported by several authors.[21,22]

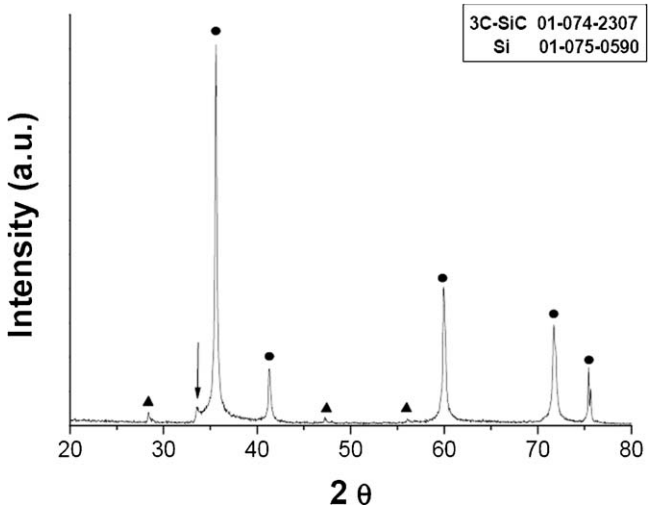

Fig. 9. XRD pattern of the ball-milled sintered sample (● = 3C-SiC, ▲ = Si).

In the as-produced powder, these stacking faults are not observed. As peaks obtained from XRD are broadened by the small average particle size, a small amount of these stacking faults could be present but remain unobservable.

After sintering, grain growth may allow the stacking faults appearance in XRD by two phenomena. On the one hand, if we consider that stacking faults are already present in the starting material but are not seen in XRD because of the broadening of the peaks, the narrowing of the peaks generated by the increase of the crystallite size upon sintering could allow the observation of the reflections due to the stacking faults. Normally these stacking faults, when present in the raw material, can be eliminated as grain growth takes place.[23] But their elimination takes place only at high temperatures[24] and, in this particular case where the applied pressure and sintering temperature hinder the excessive grain growth, the processing conditions could also impede the elimination of the stacking faults.

On the second hand, if we consider that the starting powder is free of stacking faults, the appearance of the corresponding features in XRD could be related to the formation of such defects during the crystallite growth or during the crystallization of SiC through carboreduction of the starting silica content.

The presence of defects after sintering was also corroborated by calculating the average crystallite size from peak broadening by applying the Scherer's formula. Value of around 66 nm was obtained for sample MS 1900 °C, which has to be compared to the mean grain size determined by SEM observation around 240 nm (see Fig. 8a). This value confirms the presence of defects (twinning boundaries or stacking defaults) within the grains, as reviewed by Vaβen et al.,[19] forming smaller coherent diffraction domains in the grain lattice (i.e. crystallites).

3.5. Mechanical properties

Samples were subjected to mechanical characterization (hardness, toughness) in order to correlate the final microstructures with the mechanical behavior. The influence of grain size on the hardness has been investigated. Hardness often follows the Hall-Petch relationship:

$$H_v = \sigma_o + k_o \cdot d^{-\frac{1}{2}} \quad (3)$$

where H_v is the Vickers hardness, σ_o and k_o are constants and d is the grain size.

Fig. 10 shows the evolution of hardness as a function of grain size. From the data, it seems that hardness is strongly dependent on the density and grain size as expected. The combination of both factors determined the measured values. This phenomenon may explain the differences found between hardness values. However, due to the high error levels, it is difficult to reach a conclusion about the effects of density and grain size.

A hardness gradient between the border and the center of the pellet was found. This phenomenon is induced by the density gradient caused by the forming and sintering methods.

Indeed, up to the maximum value (25 ± 0.2 GPa), hardness increases as a function of the density. Inversely, samples sintered over 1800 °C showed a slight decrease of hardness (when grain

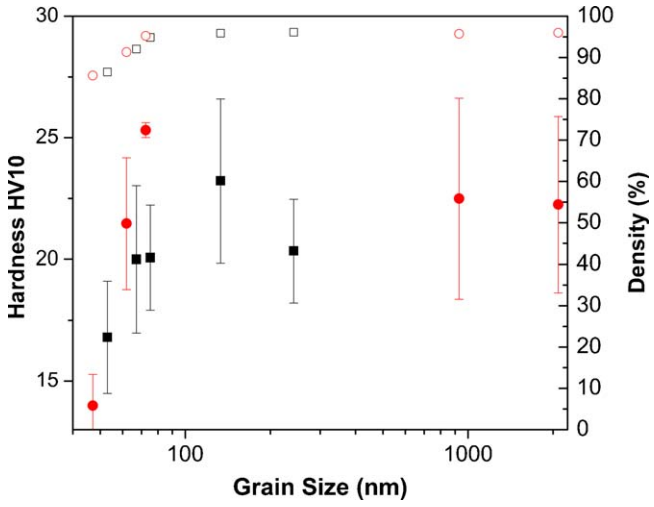

Fig. 10. Variation of Vickers hardness and relative density as a function of grain size (■ = magnetic stirring, ● = ball-milling – full coloured: hardness, non-coloured: density).

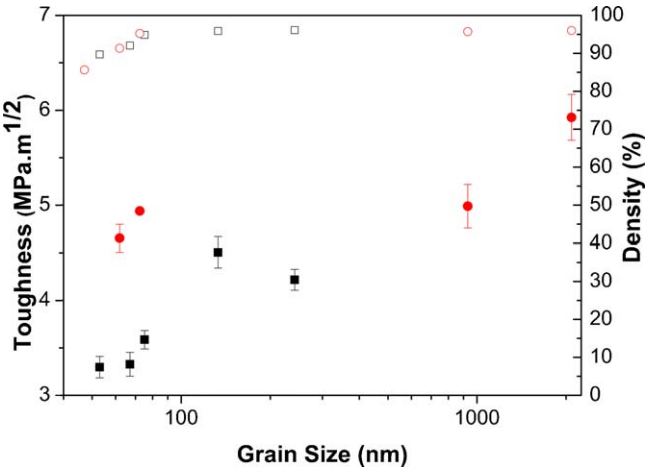

Fig. 11. Variation of fracture toughness and relative density as a function of grain size (■ = magnetic stirring, ● = ball-milling – full coloured: hardness, non-coloured: density).

sizes are >200 nm and densities >95% TD), thus following the Hall-Petch relation.

Fracture toughness was determined by direct crack measurement method using the Anstis's formula (Eq. (4)) as reported by the author.

$$K_{IC} = A\left(\frac{E}{H}\right)^{\frac{1}{2}}\left(\frac{P}{C^{\frac{2}{3}}}\right) \quad (4)$$

where c is the length of the crack from the center of the impression, A is a geometric constant equal to 0.016, P is the change expressed in Newtons, H is the hardness value and E the Young's modulus. For the calculation, the variation of the elastic modulus as a function of porosity V_p as proposed by Snead et al.[25] has been taken into account

$$E = E_o exp\,(-CV_P) \quad (5)$$

where E_o is the elastic modulus of the pore free SiC (460 GPa) and C is a constant (3.57).

As illustrated in Fig. 11, samples with grain sizes over 200 nm exhibited the highest toughness (6 ± 0.2 MPa.m$^{1/2}$).

4. Discussion

As reported in literature, hardness increases with the decreasing grain size as it has been observed in oxide and non-oxide ceramics.[26–28] However, in fine grained brittle materials a decrease of hardness can be observed when there is a residual porosity.[29] This phenomenon may explain the differences found between hardness values.

As a comparison, Yamamoto et al.[16] measured a constant hardness value of around 20 GPa in SiC materials synthetized by mechanical alloying and densified by SPS at a lower pressure 70 MPa without sintering additives. In their particular case the Hall-Petch relation has not been confirmed as authors claimed that an insufficient grain bonding was found in samples due to the absence of sintering additives. Moreover, a similar trend was observed in our study for grain sizes under 130 nm. Under this boundary, hardness seems to be ruled by the density. By increasing the grain size over 130 nm there is a slight reduction imputed to grain coarsening. This fact is less evident in BM sample, in which the influence of density in hardness seems to be stronger, with a value around 22 GPa.

With sintering additives (1 wt% bore-black carbon) Vaβen[19] measured high hardness values in SiC dense samples with grain sizes below 150 nm. Those samples prepared by HIP exhibited higher hardness values of around 26 GPa for SiC materials.

Regarding toughness, it is well known that it is strongly influenced by the microstructure. Particularly, in monolithic ceramics the average grain size determines the fracture toughness, as fracture morphology changes from intergranular to transgranular.[30]

Moreover, toughness is improved by reinforcement mechanisms such as crack bridging, microcracking and the phase transformation or the combination of these phenomena. It is supposed that these mechanisms are responsible for absorbing the available crack propagation energy.

During cracking, bridges formed by matrix grains remain intact behind the crack tip. Such bridges are formed by crack bridging of microcrack. The bridging component essentially depends on the grain size and on the frictional pullout of these grains. The frictional pullout energy (J) is considered to be proportional to the maximum crack opening displacement, $d/2$, as reviewed by Becher et al.[31] The grain bridging toughening is equal to:

$$\Delta J^{gb} = \frac{V_{gb}\tau_{gb}d}{2} \quad (6)$$

where V_{gb} is the fraction of bridging grains, τ_{gb} the frictional shear stress involved during cracking and d is the grain size. The fracture toughness (K^m) including the average fracture toughness of the various crystallographic fracture planes (J_o) is:

$$K^m = \left[E^m\left(J_o + \Delta J^{gb}\right)\right]^{\frac{1}{2}} \quad (7)$$

where E^m is the Young's modulus. The increasing of toughness as a function of grain size was reported by several authors.[32] Moreover, Rice et al.[33] showed that toughness increases as crack length increases up to a critical grain size.

Regarding our materials, higher values were obtained in comparison with the results published by Vaβen, who measured 4.2 MPa.m$^{1/2}$ by using the Evans's method.[19]

Furthermore, SiC nanocomposites prepared in absence of sintering additives presented a value of 2.2 MPa m$^{1/2}$. In this particular study, the authors employed the SEPB method for measuring.

5. Conclusions

The consolidation of SiC nanopowders synthesized by laser pyrolysis and sintered by spark plasma sintering has been investigated. A good densification (≈96% TD) was achieved by this technique in absence of sintering additives, taking into account the possible nuclear application.

By varying the sintering temperature from 1700 to 1900 °C, a different microstructural development was obtained for both dispersion routes. The ball-milling process was effective in activating the surface. Indeed, an important grain coarsening was observed in ball-milled samples at high temperature regime.

Samples exhibited interesting mechanical properties: hardness (25 GPa) and toughness (6 MPa.m$^{1/2}$). It was corroborated that the grain size, as well as the porosity strongly affected the mechanical properties. For this reason, it seems that the control of oxygen content is the key in enhancing the mechanical properties of these nanostructured carbide ceramics.

As a future activity, SiC nanoceramics should be prepared by handling powders in controlled atmosphere and dispersing the powders in organic medium, with the aim of avoiding the surface oxidation.

Acknowledgements

The authors wish to thank Aurélie Habert for SEM observations. Jocelyne Marciano (Horiba Scientific, Application laboratory, 16-18 rue du Canal, 91165 LongjumeauCedex, France) is also greatly acknowledged for chemical analyses. The authors are also grateful to Zschimmer& Schwarz GmbH & Co KG, Lahnstein for providing Dolapix samples. This work was granted by French national research agency (ANR) in the frame of the project "Silicarbitube", and by CEA Advanced Materials cross-divisions program.

References

1. Verall RA, Vlajic MD, Krstic VD. Silicon carbide as an inert-matrix for a thermal reactor fuel. *J Nucl Mater* 1999;**274**:54–60.
2. Dienst W, Fett T, Heidinger R, Rohrig HD, Schulz B. Investigation on ceramic materials for fusion technology. *J Nucl Mater* 1990;**174**:102–9.
3. Bolt H. Nonmetallic materials for plasma facing and structural applications in fusion reactors. *Fusion Eng Des* 1993;**22**:85–98.
4. Vaβen R, Kaiser A, Stover D. Potential of nanocrystalline low-Z materials for plasma facing, structural applications in fusion reactors. *J Nucl Mater* 1996;**233/237**:708–12.
5. Rose M, Balogh AG, Hahn H. Instability of irradiation induced defects in nanostructured materials. *Nucl Instrum Methods Phys Res B* 1997;**127/128**:119–22.
6. Vaβen R, Kaiser A, Forster J, Buckremer HP, Stover D. Densification of ultrafine SiC powders. *J Mater Sci* 1996;**31**:3623–37.
7. Leconte Y, Maskrot H, Combemale L, Herlin-Boime N, Reynaud C. Application of the laser pyrolysis to the synthesis of SiC TiC and ZrC pre-ceramics nanopowders. *J Anal Appl Pyrol* 2007;**79**: 465–70.
8. Cannon WR, Danforth SC, Flint JH, Hagerty JS, Marra RA. Sinterable ceramic powders from laser driven reactions: I, process description and modeling. *J Am Ceram Soc* 1982;**65**:324–30.
9. Cannon WR, Danforth SC, Flint JH, Hagerty JS, Marra RA. Sinterable ceramic powders from laser driven reactions: I, powder characteristics and process variables. *J Am Ceram Soc* 1982;**65**:330–5.
10. Cauchetier M, Croix O, Luce M. Laser synthesis of silicon carbide powders from silane and hydrocarbon mixtures. *Adv Ceram Mater* 1988;**3**: 548–52.
11. Bowen P, Carry C. From powders to sintered pieces: forming, transformation and sintering of nanostructured ceramics oxides. *Powder Technol* 2002;**128**:248–55.
12. Mayo MJ. Processing of nanocrystalline ceramics from ultrafine particles. *Int Mater Rev* 1996;**41**:85–115.
13. Palmero P, Bonelli B, Lomello F, Garrone E, Montanaro L. Role of the dispersion route on the phase transformation of a nano-crystalline transition alumina. *J Therm Anal Calorim* 2009;**97**:223–9.
14. Ohyanagi M, Yamamoto T, Kitaura H, Kodera Y, Ishii T, Munir Z. Consolidation of nanostructured SiC with disorder-order transformation. *Scripta Mater* 2004;**50**:114.
15. Tamari N, Tanaka T, Tanaka K, Kondoh I, Kawahara M, Tokita M. Effect of spark plasma sintering on densification and mechanical properties of silicon carbide. *J Ceram Soc Jpn* 1995;**103**:740–2.
16. Yamamoto TA, Kondou T, Koder Y, Ishii T, Ohyanagi M, Munir Z. Mechanical properties of β-SiC fabricated by spark plasma sintering. *J Mater Eng Perform* 2005;**14**:460–6.
17. Anstis GR, Chantikul P, Lawn BR, Marshall DB. A critical evaluation of indentation techniques for measuring fracture toughness: I direct crack measurements. *J Am Ceram Soc* 1981;**64**:533–8.
18. National Institutes of Health. ImageJ. http://rsb.info.nih.gov/ij. 12 August 2011.
19. Vaβen R, Stover D. Processing and properties of nanograin silicon carbide. *J Am Ceram Soc* 1999;**82**:2585–893.
20. Van Rijswijk W, Shanefield DJ. Effects of carbon as a sintering aid in silicon carbide. *J Am Ceram Soc* 1990;**73**:148–9.
21. Tatayema H, Sutoh N, Mukarawa N. Quantitative analysis of stacking faults in the structure of SiC by X-ray powder profile refinement method. *J Ceram Soc Jpn* 1988;**96**:1003–11.
22. Hao YJ, Jin GQ, Han XD, Guo XY. Synthesis and characterization of bamboo-like SiC fibers. *Mater Lett* 2006;**60**:1334–7.
23. Gubicza J, Nauyoks S, Balogh L, Labar J, Zerda TW, Ungar T. Influence of sintering temperature and pressure on crystallite size and lattice defect structure in nanocrystalline SiC. *J Mater Res* 2007;**22**: 1314–21.
24. Koumoto K, Takeda S, Pai CH. High-resolution electron microscopy observation of stacking faults in β-SiC. *J Am Ceram Soc* 1989;**72**: 1985–7.
25. Snead LL, Nozawa T, Katoh Y, Byun TS, Kondo S, Petti DA. Handbook of SiC properties for fuel performance modeling. *J Nucl Mater* 2007;**371**:329–77.
26. Bellosi A, Sciti D, Guicciardi S. Synergy and competition in nano- and micro- design of structural ceramics. *J Eur Ceram Soc* 2004;**24**: 3295–302.
27. Krell A, Blank P. Grain size dependence of hardness in dense submicrometer alumina. *J Am Ceram Soc* 1995;**78**:1118–20.
28. Rice RW, Wu CC, Borchelt F. Hardness-grain-size relations in ceramics. *J Am Ceram Soc* 1994;**77**:2539–53.
29. Hahn H, Padmanabhan KA. Mechanical reponse of nanostructured materials. *Nanostruct Mater* 1995;**6**:191–200.

30. Conner CL, Faber KT. Segregant-enhanced fracture in magnesium oxide. *J Mater Sci* 1990;**25**:2737–3742.
31. Becher PF, Fuller ER, Angelini P. Matrix-grain-bridging contribution to the toughness whisker-reinforced ceramics. *J Am Ceram Soc* 1991;**74**:2131–5.
32. Becher PF. Microstructural design of toughened ceramics. *J Am Ceram Soc* 1991;**74**:255–69.
33. Rice RW, Freiman SW, Becher PF. Grain size dependence of fracture energy in ceramics, I experiments. *J Am Ceram Soc* 1981;**64**:345–50.